

Weak and vanishing upper mantle discontinuities generated by large-scale lithospheric delamination in the Longmenshan area, China

Chuansong He (✉ hechuansong@aliyun.com)

Institute of Geophysics, CEA

Research Article

Keywords: Longmenshan, lithospheric delamination, tomography, CCP stacking of receiver functions, 410 km discontinuity, 660 km discontinuity

Posted Date: July 13th, 2021

DOI: <https://doi.org/10.21203/rs.3.rs-710024/v1>

License:  This work is licensed under a Creative Commons Attribution 4.0 International License.

[Read Full License](#)

1 **Weak and vanishing upper mantle discontinuities generated**
2 **by large-scale lithospheric delamination in the Longmenshan**
3 **area, China**

4

5 Chuansong He^{1*}

6 Institute of geophysics, China Earthquake Administration, 100081, Beijing

7

8 **Abstract:** A large amount of high-quality teleseismic data is used for common conversion
9 point (CCP) stacking of receiver functions in the Longmenshan area. The results show
10 that a large-scale high-velocity anomaly or lithospheric delamination can completely
11 destroy upper mantle discontinuities or erase the phase boundary of olivine, which is a
12 very important finding and can be used to assess stagnant slabs in the mantle transition
13 zone globally. The deepening region of the 660 km discontinuity beneath the
14 Songpan-Ganzi terrane might indicate that the large-scale high-velocity anomaly in the
15 mantle transition zone is a cold domain and can affect the topography of upper mantle
16 discontinuities.

17 **Key words:** Longmenshan, lithospheric delamination, tomography, CCP stacking of
18 receiver functions, 410 km discontinuity, 660 km discontinuity.

* Corresponding author: Chuansong He (hechuansong@aliyun.com)

19

20 **Plain language summary:** *In this study, a large amount of high-quality teleseismic data is*
21 *used for CCP stacking of receiver functions in the Longmenshan area. The results imply a*
22 *very important finding that a high-velocity anomaly can completely destroy upper mantle*
23 *discontinuities or greatly erase the phase change in olivine. The deepening region of the*
24 *660 km discontinuity beneath the Songpan-Ganzi terrane might indicate that the*
25 *large-scale high-velocity anomaly in the mantle transition zone is a cold domain and can*
26 *affect the topography of upper mantle discontinuities.*

27

28 **1. Introduction**

29

30 The Longmenshan region has undergone two orogenic events since the Mesozoic:
31 east-west deformation induced by the Indosinian orogeny in the Late Triassic–Early
32 Jurassic (Roger et al., 2008) and south-north deformation linked to the collision between
33 the Indian and Asian continents in the Cenozoic (Zhang et al., 2020; Tong et al., 2021).
34 This collision has subsequently led to large-scale crustal shortening across Asia and
35 greatly deformed the Longmenshan area (e.g., Molnar and Tapponnier, 1975; Chatterjee
36 et al., 2013; Searle, 1995; Huang et al., 2005).

37

38 GPS studies have reported that crustal materials are moving eastward from the
39 Tibetan Plateau into the Longmenshan area in the Cenozoic (Zhang et al., 2004), but they
40 are obstructed by the rigid crust and lithosphere of the Yangtze block or the Sichuan Basin
41 (e.g., Copley and McKenzie, 2007; Oskin, 2012). This might result in stress accumulation
42 and release in this area (He et al., 2019) and lead to several devastating earthquakes in
43 the Longmanshan area, such as the 2001 Mw 7.8 Kunlun, the 2008 Mw 7.9 Wenchuan,
44 the 2010 Mw 6.9 Yushu and the 2013 Ms 7.0 Lushan earthquakes.

45

46 Tomography has revealed the absence of the lithosphere beneath the
47 Songpan-Ganzi terrane and large-scale lithospheric delamination in the Longmenshan
48 area (He et al., 2019), which might have played a key role in stress accumulation and
49 release and facilitated the eastern extrusion of the Tibetan Plateau (Tian et al., 2021) as
50 well as ductile crustal thickening (Burchfiel et al., 2008; Chang et al., 2012). However, this
51 work provides only one piece of evidence. Therefore, it is necessary to further investigate
52 and confirm this deep process.

53

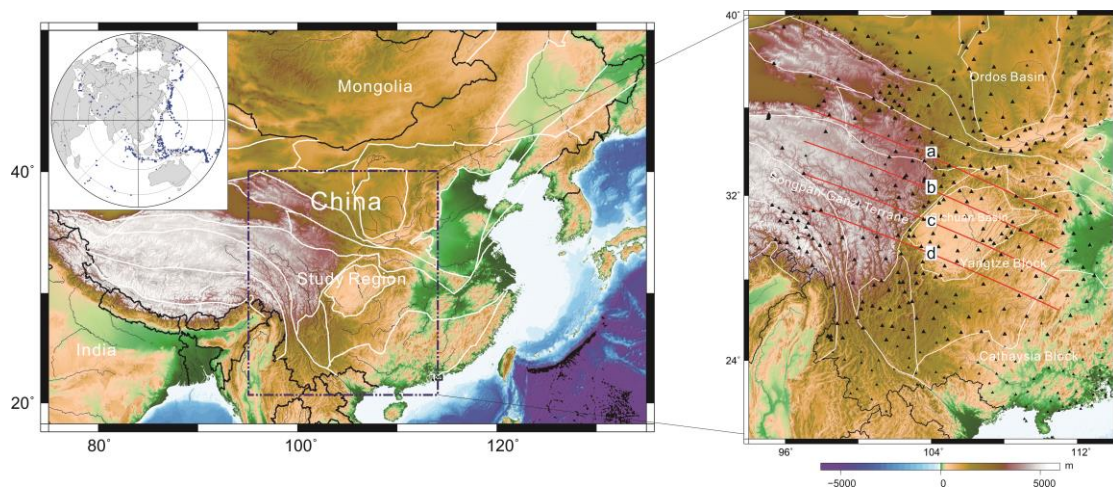
54 Based on tomographic images, the lithospheric structure (or a large-scale
55 low-velocity structure) has delaminated into the MTZ beneath the Songpan-Ganzi terrane
56 (He et al., 2019). Generally, a high-velocity anomaly is a cold domain, which might induce
57 structural variations in the mantle transition zone (MTZ) (Foulger, 2012). The receiver

58 function technique is an effective tool that can be used to detect the structure of the MTZ.
59 Accordingly, I collected a large amount of high-quality teleseismic data, carried out
60 common conversion point (CCP) stacking of receiver functions and imaged the structure
61 of the MTZ. The results show that a large-scale high-velocity anomaly can result in weak
62 and vanishing upper mantle discontinuities and demonstrate that the lithosphere has
63 delaminated into the MTZ.

64

65 2. Data and method

66



67

68 Fig. 1 Left panel: location of the study region; inset figure: distribution of events used in
69 this study. Right panel: distribution of seismic stations and tectonic framework; white lines:
70 boundaries of geological units; red lines: profiles for CCP stacking of receiver functions;
71 profiles b and c also show P-wave velocity perturbations (He et al., 2019).

72

73 In total, 684 teleseismic events were collected from 406 permanent seismic
74 stations recorded during 2007-2020 (Fig. 1), with earthquake epicentral distances ranging
75 from 30° to 90° for individual event-station pairs and $M_s > 6.0$ (Fig. 1, insert in left panel).
76 The raw record was cut from 15 s before to 200 s after the P-wave arrival and filtered by a
77 Butterworth bandpass filter between 0.05 and 1 Hz. To select consistent raw data for the
78 waveforms, a cross-correlation technique (VanDecar and Crosson, 1990) was used for
79 data processing (for example, see Fig. S1). Finally, 16258 high-quality receiver functions
80 were extracted by a modified frequency-domain deconvolution (0.01 water level and 1 Hz
81 Gaussian filter) (Zhu and Kanamori, 2000; Langston, 1979) (for example, see Fig. S2).

82

83 The technique of CCP stacking of receiver functions is employed to define the
84 topographies of the 410 and 660 km discontinuities (e.g., Eagar et al., 2010; Zhu, 2000;
85 Xu et al., 2018), and spherical coordinates are established to calculate the Ps-P
86 differential time T_{Ps} (Eagar et al., 2010):

87

$$88 \quad T_{Ps} = \sum_i^N \left(\sqrt{\left(\frac{R_i}{V_{Si}}\right)^2 - p_{Ps}^2} - \sqrt{\left(\frac{R_i}{V_{Pi}}\right)^2 - p_P^2} \right) \frac{\Delta r}{R_i} \quad (1)$$

89

90 where the ray parameters of the direct Ps and P phases are represented as p_{Ps} and
91 p_P , respectively. V_{Pi} and V_{Si} are the P- and S-wave velocities in the i th layer, and R_i and Δr
92 represent the Earth's semidiameter at each i th depth shell (r_i) and depth interval. A 3-D
93 global P- and S-wave velocity model by Lu et al. (2019) is used to remove the velocity
94 heterogeneity effects in the upper mantle. The Ps-P differential times in the 3-D model are
95 presented as follows:

96

$$97 \quad T_{Ps3D} = T_{Ps} + \Delta T \quad (2)$$

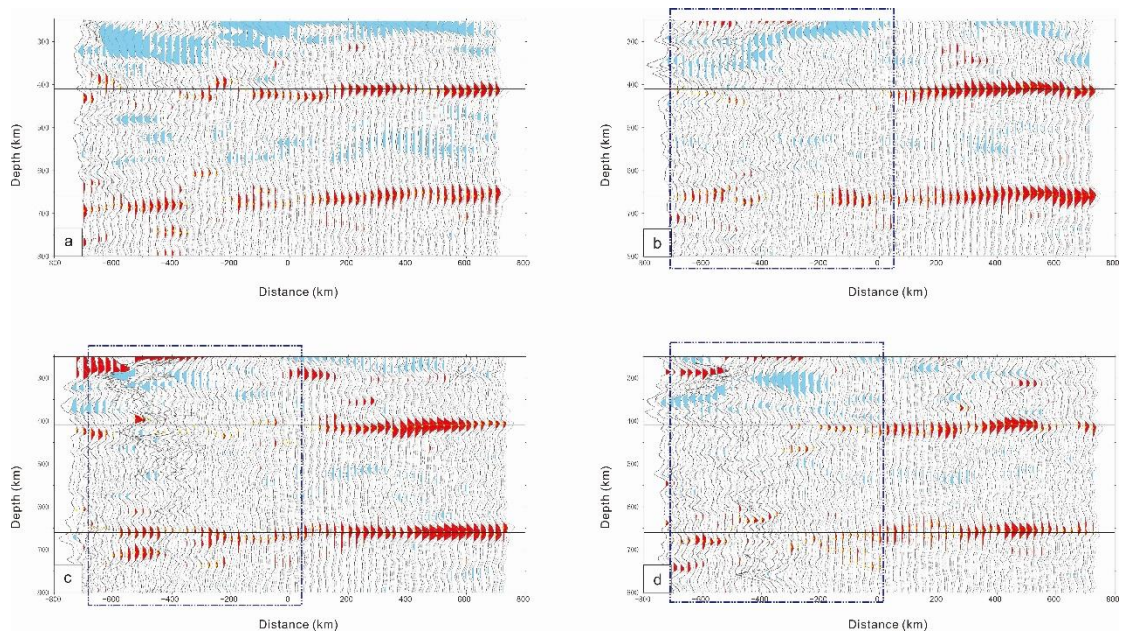
98

99 where ΔT is related to the travel-time correction or the 3-D velocity perturbations.
100 The high- and low-velocity anomalies in the upper mantle can result in a travel-time
101 increase or decrease (ΔT) of a ray and lead to deviations in the real depths of the 410 and
102 660 km discontinuities. In the CCP stacking of receiver functions, the lateral grid interval
103 and depth interval are designed as 0.5° and 1 km, respectively, and the search radius (or
104 bin) of the migrated receiver functions is designated as 75 km (Xu et al., 2018). In each
105 bin, bootstrap resampling with 2000 resampling iterations (Efron and Tibshirani, 1986) is
106 used to calculate the mean value and standard deviation. Piercing points are calculated
107 by the 1-D AK135 velocity model (Kennett et al., 1995), which shows good and
108 reasonable piercing point distributions at the depths of the 410 and 660 km (Fig. S3).

109

110 **3. Results and discussion**

111



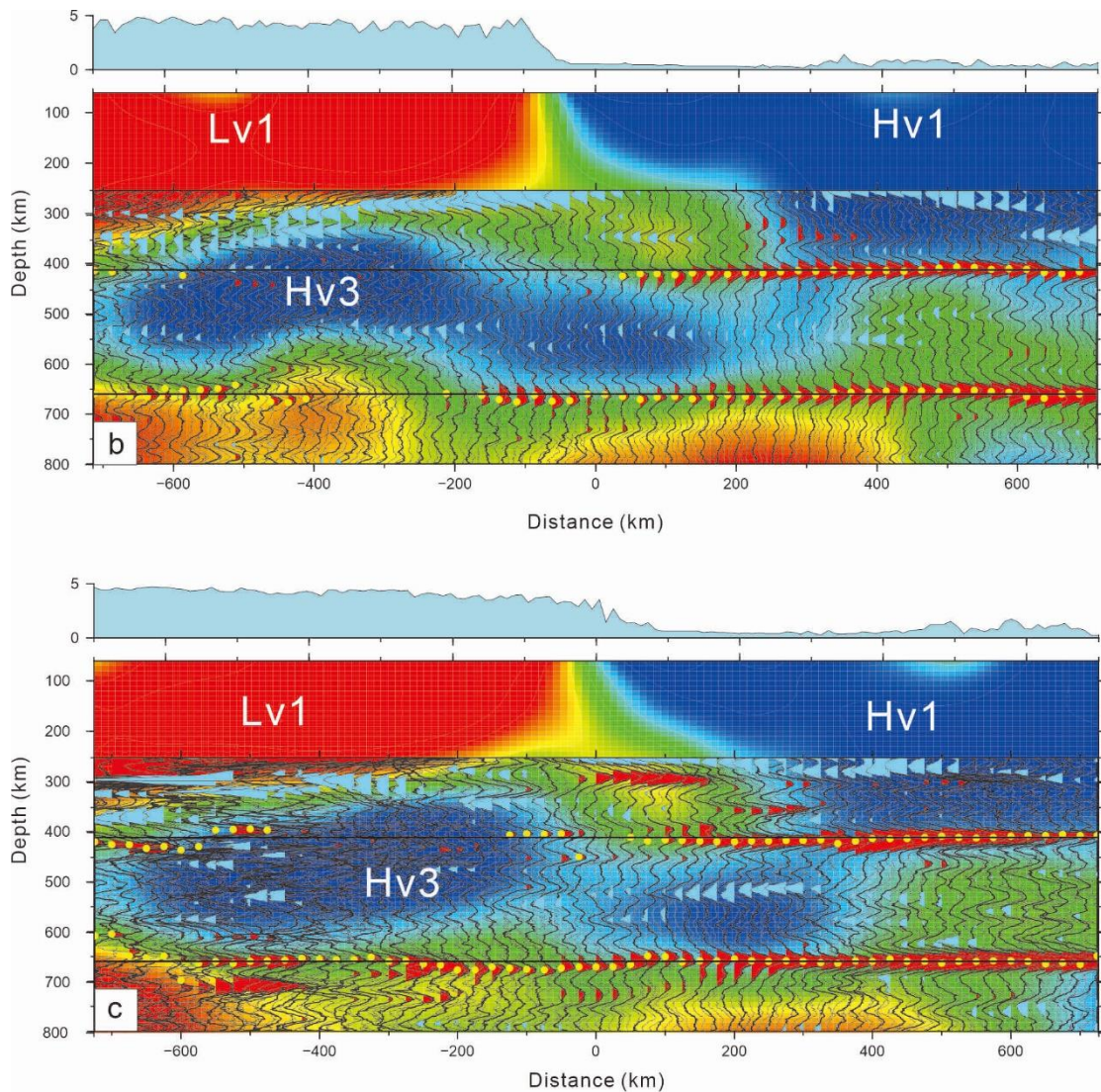
112

113 Fig. 2 CCP stacking profiles of receiver functions (a-d) corrected by a 3-D global P- and
114 S-wave velocity model (Lu et al., 2019). Blue rectangular region: weak and vanishing 410
115 km and 660 km discontinuities. The yellow points are picked for the depths of both the 410
116 km and 660 km discontinuities on the CCP stacking of receiver functions. The
117 bootstrapping method with 2000 stacked amplitudes is used to resample and calculate the
118 dataset, and the final mean receiver functions corresponding to the 95% confidence level
119 are calculated. Horizontal blue lines: depths of 410 and 660 km.

120

121 Four CCP stacking profiles of receiver functions were obtained (Fig. 2; for the
122 locations of the profiles, see Fig. 1). The results show that the amplitude of the 410 km

123 discontinuity becomes small in the western part of profile a, whereas the 410 km
124 discontinuity almost vanishes in the western parts of profiles b, c and d. Moreover, the
125 local 660 km discontinuity also vanishes in the western parts of profiles b, c and d.



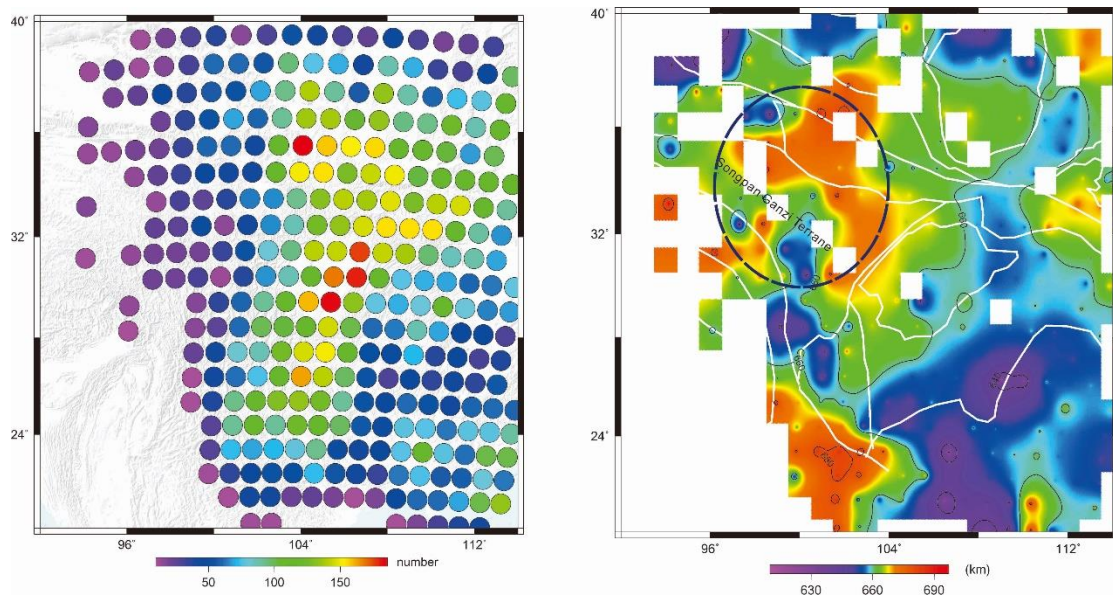
126
127 Fig. 3. Profiles b and c. Overlapping diagram of the P-wave velocity perturbation (He et al.,
128 2019) and the CCP stacking profiles (profiles c and d; see the locations in Fig. 1). A weak
129 or vanishing 410 km discontinuity corresponds to the high-velocity anomaly (Hv3) or
130 large-scale lithospheric delamination. The yellow points are picked for the depths of both
131 the 410 km and 660 km discontinuities in the CCP stacking of receiver functions. The

132 bootstrapping method with 2000 stacked amplitudes is used to resample and calculate the
133 dataset, and the final mean receiver functions corresponding to the 95% confidence level
134 are calculated. Horizontal blue lines: depths of 410 and 660 km.

135

136 To further check this issue, P-wave velocity perturbation profiles overlap with the CCP
137 stacking profiles (b and c) (Fig. 3). The results indicate that the vanishing 410 km
138 discontinuity in the western parts of profiles b and c corresponds well to the high-velocity
139 anomaly (Hv3) (He et al., 2019). Clearly, the large-scale high-velocity anomaly (Hv1)
140 completely destroys the 410 km discontinuity or makes the phase boundary of olivine
141 vanish. To date, no such case has been reported anywhere in the world.

142



144 Fig. 4. Left panel: CCP stacking points of receiver functions, which are corrected by a 3-D
145 global P- and S-wave velocity model (Lu et al., 2019). A stacking point with more than 10
146 points can be used to calculate the depth of the 660 km discontinuity. Blue elliptical region:
147 the deepening region of the 660 km discontinuity.

148

149 I have attempted to extract the topographies of the 410 km and 660 km
150 discontinuities. However, due to the weak and vanishing 410 km discontinuity in the
151 western part of the study region, obtaining the complete topography of the 410
152 discontinuity is very difficult. Accordingly, I extract the topography of only the 660 km
153 discontinuity in this area (Fig. 4). The results show that the 660 km discontinuity beneath
154 the Songpan-Ganzi terrane is deepened by an average of approximately 20-30 km (Fig. 4,
155 right panel: blue elliptical region) compared to the global topography of the 660 km
156 discontinuity (e.g., Flanagan and Shearer, 1999; Houser et al., 2008).

157

158 Experimental studies have revealed that upper mantle discontinuities might be
159 associated with phase changes in olivine (Katsura and Ito, 1989; Ringwood, 1975). The
160 410 km discontinuity has a positive pressure-temperature slope that involves the
161 olivine-to-wadsleyite transition (Helfrich, 2000), whereas the 660 km discontinuity exhibits
162 a negative pressure-temperature gradient that involves the ringwoodite phase
163 transformation to perovskite and magnesiowüstite (Helfrich, 2000; Bina and Helfrich,

164 1994; van der Meijde et al., 2005). A high-velocity anomaly is generally considered a
165 lower-temperature domain than the surrounding mantle; thus, inferring that the deepening
166 topography of the 660 km discontinuity beneath the Songpan-Ganzi terrane might be
167 associated with the low-velocity anomaly (Hv3).

168

169 **4. Conclusion**

170

171 Weak and vanishing upper mantle discontinuities correspond well to large-scale
172 high-velocity anomalies, which might indicate or demonstrate that the lithosphere has
173 delaminated into the mantle transition zone. An important finding is that large-scale
174 high-velocity anomalies or lithospheric delamination can completely destroy upper mantle
175 discontinuities or make them vanish. This result can be used to understand or assess a
176 stagnant slab in the mantle transition zone, which is an issue that generates great
177 controversy.

178

179 **Acknowledgments**

180

181 I am grateful to the National K&D Plan of China (Grant No. 2017YFC601406). The raw
182 data used for CCP stacking of receiver functions can be accessed at
183 <https://doi.org/10.5281/zenodo.5035828>.

184

185

186 **References**

187

- 188 Bina, C. & Helffrich, G. (1994). Phase transition Clapeyron slopes and transition zone
189 seismic discontinuity topography. *J Geophys. Res.*, *99*, 15853-15860.
- 190 Burchfiel, B. C., Royden, L. H., van der Hilst, R. D., Hager, B. H., Chen, Z., King, R. W., Li,
191 C., Lu, J., Yao, H. & Kirby, E. (2008). A geological and geophysical context for the
192 Wenchuan earthquake of 12 May 2008, Sichuan, China. *GSA Today* *18* (7), 4-11.
- 193 Chang, C. P., Chen, G. H., Xu, X. W., Yuan, R. M., Kuo, Y. T. & Chen, W. S. (2012).
194 Influence of the pre-existing Xiaoyudong salient in surface rupture distribution of the
195 Mw 7.9 Wenchuan earthquake, China. *Tectonophysics* *530–531*, 240-250.
- 196 Chatterjee, S., Goswami, A. & Scotese, C. R. (2013). The longest voyage: Tectonic,
197 magmatic, and paleoclimatic evolution of the Indian plate during its northward flight
198 from Gondwana to Asia. *Gondwana Research* *23*, 238-267.

199 Copley, A. & McKenzie, D. (2007). Model of crustal flow in the India-Asia collision zone.
200 *Geophysical Journal International* 169, 683-698.

201 Eagar, K. C., Fouch, M. J. & James, D. E. (2010). Receiver function imaging of upper
202 mantle complexity beneath the Pacific Northwest, United States. *Earth Planet. Sci.*
203 *Lett.*, 297, 141-153.

204 Efron, B. & Tibshirani, R. B. (1986). Bootstrap methods for standard errors, confidence
205 intervals, and other measures of statistical accuracy. *Stat. Sci.*, 1, 54-75.

206 Flanagan, M. P. & Shearer, P. M. (1999). A map of topography on the 410-km
207 discontinuity from PP precursors. *Geophys. Res. Lett.*, 26, 549-552.

208 Foulger, G. R. (2012). Are 'hot spots' hot spots?. *J. Geodyn.*, 58, 1-28.

209 He C. S., Dong, S. W. & Wang, Y. H. (2019). Lithospheric delamination and upwelling
210 asthenosphere in the Longmenshan area: insight from teleseismic p-wave
211 tomography. *Scientific Reports*, 9, 6967.

212 Helffrich, G. (2000). Topography of the transition zone seismic discontinuities. *Rev.*
213 *Geophys.*, 38, 141-158.

214 Houser, C., Masters, G., Shearer, P. M. & Laske, G. (2008). Shear and compressional
215 velocity models of the mantle from cluster analysis of long-period waveforms.
216 *Geophys. J. Int.*, 174, 195-212.

217 Huang, B. C., Piper, J. D. A., Wang, Y. C., He, H. Y. & Zhu, R. X. (2005). Paleomagnetic
218 and geochronological constraints on the post-collisional northward convergence of
219 the southwest Tian Shan, NW China. *Tectonophysics*, 409, 107-124.

220 Katsura, T. & Ito, E. (1989). The system Mg_2SiO_4 – Fe_2SiO_4 at high pressures and
221 temperatures: precise determination of stabilities of olivine, modified spinel, and
222 spinel. *J. Geophys. Res.*, 94, 15663-15670.

223 Kennett, B. L. N., Engdahl, E. R. & Buland, R. (1995). Constraints on seismic velocities in
224 the Earth from traveltimes. *Geophys. J. Int.*, 122, 108-124.

225 Langston, C. A. (1979). Structure under Mount Rainier, Washington, inferred from
226 teleseismic body waves. *J. Geophys. Res.*, 84, 4749-4762.

227 Molnar, P. & Tapponnier, P. (1975). Cenozoic tectonics of Asia: effects of a continental
228 collision. *Science*, 189 (4201), 419-426.

229 Oskin, M. E. (2012). Reanimating eastern Tibet. *Nature Geoscience*, 5, 597-598.

230 Owens, T. J., Zandt, G. & Taylor, S. R. (1984). Seismic evidence for an ancient rift
231 beneath the Cumberland Plateau, Tennessee: a detailed analysis of broadband
232 teleseismic P waveforms. *Journal of Geophysical Research* 89, 7783-7795.

233 Ringwood, A. (1975). Composition and Petrology of the Earth's Mantle. McGraw-Hill, New
234 York 618.

235 Roger, F., Jolivet, M. & Malavielle, J. (2008). Tectonic evolution of the Triassic fold belts of
236 Tibet. *Comptes Rendus Geoscience*, 340, 180-189.

237 Searle, M. (1995). The rise and fall of Tibet. *Nature* 374, 17-18.

238 Tian, H. Y., He, C. S. & Santosh, M. (2021). S-wave velocity structure of the
239 Sichuan-Yunnan region, China: implications for extrusion of Tibet Plateau and
240 seismic activities. *Earth and Space Science*, accepted.

241 Tong, Y., Yang, Z., Pei, J., Wang, H., Wu, Z., & Li, J. (2021). Crustal clockwise rotation of
242 the southeastern edge of the Tibetan Plateau since the late Oligocene. *Journal of*
243 *Geophysical Research*, 126, e2020JB020153.

244 van der Meijde, M., van der Lee, S. & Giardini, D. (2005). Seismic discontinuities in the
245 Mediterranean mantle. *Phys. Earth Planet. Inter.*, 148, 233-250.

246 VanDecar, J. C. & Crosson, R. S. (1990). Determination of teleseismic relative phase
247 arrival times using multi-channel cross-correlation and least squares. *Bull. Seismol.*
248 *Soc. Am.*, 80, 150-169.

249 Xu, M. J., Huang, H., Huang, Z. C., Wang, P., Wang, L. S., Xu, M.J ., Mi, N., Li, H., Yu, D.
250 Y. & Yuan, X. H. (2018). Insight into the subducted Indian slab and origin of the
251 Tengchong volcano in SE Tibet from receiver function analysis. *Earth Planet. Sci.*
252 *Lett.*, 482, 567-579.

253 Zhang, C., Guo, Z., & Chen, Y. J. (2020). Lithospheric thickening controls the ongoing
254 growth of northeastern Tibetan Plateau: Evidence from P and S receiver functions.
255 *Geophysical Research Letters*, 47, e2020GL088972.

256 Zhang, P. Z., Shen, Z., Wang, M. & Gan, W. (2004). Continuous deformation of the
257 Tibetan Plateau from Global Positioning System data. *Geology*, 32, 809-812.

258 Zhu, L. & Kanamori, H. (2000). Moho depth variation in southern California from
259 teleseismic receiver functions. *J. Geophys. Res.*, 105, 2069-2980.

260 Zhu, L. (2000). Crustal structure across the San Andreas Fault, southern California from
261 teleseismic converted waves. *Earth Planet. Sci. Lett.*, 179, 183-190.

262 **Author contributions**

263 H.C. conducted the analysis and wrote the first draft, and contributed to the interpretation
264 of results and writing.

265 **Additional information**

266 Competing Interests: The author declare no competing interests.

267 **Electronic supplementary material**

268 Supplementary Information

269

270

271

Supplementary Files

This is a list of supplementary files associated with this preprint. Click to download.

- [20210628SupplementaryInformation.docx](#)